Remote Sensing of Environment 200 (2017) 18–30

Contents lists available at ScienceDirect

Remote Sensing of Environment

journal homepage: www.elsevier.com/locate/rse

Airborne mapping of benthic reflectance spectra with Bayesian linear mixtures

David R. Thompson[a,*], Eric J. Hochberg[b], Gregory P. Asner[c], Robert O. Green[a], David E. Knapp[c], Bo-Cai Gao[d], Rodrigo Garcia[e], Michelle Gierach[a], Zhongping Lee[e], Stephane Maritorena[f], Ronald Fick[g]

[a] Jet Propulsion Laboratory, California Institute of Technology, Pasadena, CA 91109, USA
[b] Bermuda Institute of Ocean Sciences, St. George's GE 01, Bermuda
[c] Carnegie Institution for Science, Stanford, CA 94305, USA
[d] Naval Research Laboratory, USA
[e] University of Massachusetts, Boston, MA, USA
[f] University of California Santa Barbara, Santa Barbara, CA, USA
[g] University of Florida, Gainesville, FL, USA

ARTICLE INFO

Keywords:
Imaging spectroscopy
Coral reefs
Atmospheric correction
Remote sensing

ABSTRACT

Remote imaging spectroscopy from 400 to 800 nm can use benthic reflectance signatures to map the composition and condition of shallow water ecosystems. We present a novel probabilistic approach to jointly estimate the seafloor reflectance and water properties while flexibly incorporating varied domain knowledge and *in situ* measurements. The inversion transforms remote radiance data with an atmospheric correction followed by a water column correction. Benthic reflectance and water optical properties are both represented by linear mixtures of endmember spectra. We combine remote measurements, prior knowledge and field data using a flexible Bayesian optimal estimation, solving for the *Maximum A Posteriori* (MAP) combination of water column properties, seafloor reflectance, and depth. We then demonstrate performance in controlled simulations and in overflights of a coral reef in Hawaii with coincident *in situ* measurements. The measurement approach helps lay a foundation for wide-area airborne mapping of the condition of threatened coastal ecosystems such as coral reefs.

1. Introduction

Remote measurement of benthic reflectance addresses a range of compelling environmental challenges. Shallow aquatic ecosystems, including kelp beds (Bell et al., 2015), coral reefs (Andréfouët et al., 2007; Hochberg, 2011), seagrass (Chauvaud et al., 1998), and wetlands (Turpie et al., 2015), serve key roles for coastal populations and the global environment. They are sites of nutrient and material cycling, carbon storage, and transport. They act as reservoirs and incubators of biodiversity (Roberts et al., 2002; Bruckner, 2002), host coastal fishing economies (White et al., 2000), and protect human settlements from erosion. These coastal ecosystems are fragile and increasingly threatened by environmental change (Mark Eakin et al., 2010; Nicholls et al., 2007). Potential dangers include acidification (Hoegh-Guldberg et al., 2007), agricultural runoff, industrial pollution, overfishing, and invasive species. While such stressors are apparent in small-scale studies, data is insufficient to characterize regional or global scales. Remote spectroscopy can fill this gap (Hochberg et al., 2003). Solar illumination in the 400–800 nm range penetrates shallow water where the bottom reflectance, R_b, shows diagnostic spectral signatures of different surfaces and organisms. Airborne and space-based mapping spectrometers well-suited to monitor benthic ecosystems (Mumby et al., 2004). Here we focus on coral reefs, motivated by a wave of airborne campaigns by instruments such as NASA's Portable Remote Imaging SpectroMeter (PRISM) (Mouroulis et al., 2014) and the Carnegie Airborne Observatory (CAO) (Asner et al., 2012). Remote coral reef investigations use R_b signatures to discriminate bottom types including, but perhaps not limited to, coral, sand and algae, and thereby study the condition of Earth's reef ecosystems (Hochberg et al., 2003).

Remote R_b surveys on these scales will require flexibility to incorporate diverse *in situ* measurements and domain knowledge. Such constraints can mitigate many challenges of measuring R_b. One such challenge is distortion caused by the intervening atmosphere and water column (Hedley et al., 2012; Botha et al., 2013). Another is the

* Corresponding author.
E-mail address: david.r.thompson@jpl.nasa.gov (D.R. Thompson).

http://dx.doi.org/10.1016/j.rse.2017.07.030
Received 25 August 2016; Received in revised form 19 July 2017; Accepted 28 July 2017

ambiguity between glint, bottom reflectance, depth, and water optical properties which makes the R_b inversion underdetermined (Garcia et al., 2015). This is complicated by large data volumes of modern imaging spectrometers; exact per-spectrum radiative transfer is not typically possible for the increasing size of detector arrays. Instead, investigators typically use faster approximations. Dekker et al. (2011) and Zoffoli et al. (2014) review these parameterizations and retrieval methods. They generally conclude that there is no single best solution to disentangle water optical and bottom effects, and that the optimal choice depends on the availability of prior knowledge and in-situ instrumentation. Since multi-site, multi-region missions may not have comprehensive or consistent ancillary data, the retrieval should be flexible enough to incorporate whatever prior knowledge is available. This property will be important to achieve generality for operational use in wide-area benthic ecosystem mapping. The algorithms should be able to function without full set of accurate constraints, conditions under which many inversion algorithms are vulnerable to numerical instability from ill-conditioning, instability from local minima, and high sensitivity to input values.

We address this challenge with a probabilistic retrieval (Jay and Guillaume, 2014), using priors to flexibly incorporate any available ancillary data. Here optimal estimation promotes retrieval stability and incorporates soft or hard constraints on depth or water properties. The approach is commonplace for underdetermined inversions in terrestrial surface studies (Lewis et al., 2012) and atmospheric sounding (Rodgers, 2000). The Bayesian methodology is particularly appropriate for the aquatic domain (Frouin and Pelletier, 2015) since it serves as a principled and flexible framework to incorporate complementary data from *in situ* instruments. We use a classical composition of multivariate Gaussian prior and likelihood terms as described in Lewis et al. (2012).

To further support diverse field measurements we permit water column models using either Inherent Optical Properties (IOPs) or Apparent Optical Properties (AOPs). There are many existing IOP-based approaches for retrieving R_b (Dekker et al., 2011); they represent the water column using parameters derived from physically-measurable variables such as particle concentrations. AOP-based models may also be advantageous for certain studies since the equipment required to measure them *in situ* is compact and simple to deploy. To enable AOP models, we parameterize the water column with the spectrally-varying backscatter and diffuse attenuation (Maritorena et al., 1994). Following prior studies, we represent benthic reflectance by linear mixtures of library endmembers (Klonowski et al., 2007; Hamylton, 2011; Hedley et al., 2004; Dekker et al., 2011; Petit et al., 2017). We extend this concept with a similar representation for the spectrally-varying AOPs, producing a joint model that comprised a *nonlinear combination of linear mixtures*. Benthic and column parameters combine into a real-valued state vector that is optimized independently for every spectrum, as in previous inversion methods using IOP parameters (Dekker et al., 2011; Petit et al., 2017; Lee et al., 1999). Here, linear mixtures capture the relevant subspace of spectral variability. The water column, along with depth and bottom reflectance, determines the reflectance at the water surface.

Our study tests the hypothesis that this methodology can accurately retrieve R_b for reef surface classification, characterizing its performance in simulation and demonstrating its application to an airborne dataset. We first present our proposed approach and explore performance of IOP and AOP models in controlled simulations. Then, we evaluate the combined system on field datasets consisting of observations by the CAO instrument of Hawaiian coral reefs. This validation presages the potential for larger datasets such as those of the COral Reef Airborne Laboratory (CORAL), which will map coral reefs at many locations worldwide.

2. Approach

We applied radiometric and spectral calibrations to yield a spectral image of radiances at each wavelength channel, and then analyzed each spectrum using a three step inversion of atmosphere, surface, and water column (Fig. 1). We first corrected atmospheric effects with an approach similar to that of Thompson et al. (2015a); Gao et al. (1993). Specifically, we estimated atmospheric aerosol content and then inverted scattering and transmission effects to recover remote sensing reflectance, R_{rs}, at the water surface. We next corrected for surface effects including refraction and sunglint. Finally, we used a numerical inversion of several water column models to estimate benthic reflectance. An AOP variant expanded the linear mixture idea to model both water and bottom properties, with a real-valued $\mathbb{R}^N$ vector representation of all free parameters. This enabled a single joint retrieval of AOPs, depth, and R_b over a wide range of conditions using gradient descent. We used the same strategy for jointly retrieving benthic reflectance mixtures and the scalar HOPE parameters of H, G, B, P, and X (Lee et al., 1999). For both models, the calculation was fast, with no need for runtime radiative transfer models, and stable, providing a well-conditioned solution that was robust to initialization conditions and local minima. Critically, the approach permitted Bayesian regularization to incorporate "soft" constraints from *in situ* measurements (Lewis et al., 2012).

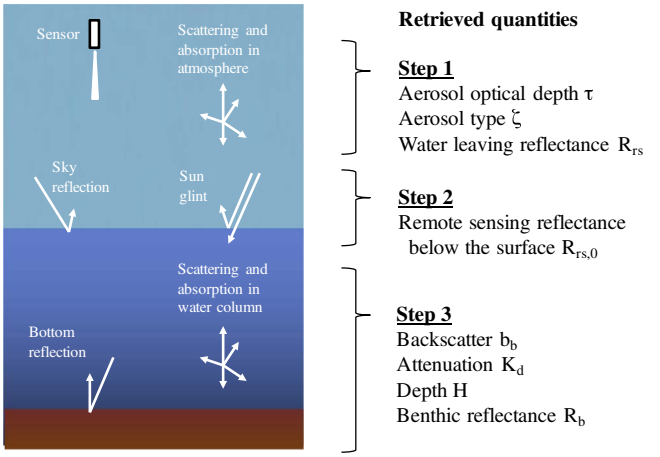

Fig. 1. Estimating R_b from remotely-sensed radiance is a multi-step process involving many intermediate quantities.

2.1. Remote sensing reflectance

Our atmospheric correction used a modified version of the ATmospheric REMoval (ATREM) approach by Gao et al. (Gao and Goetz, 1990; Gao et al., 1993) and further expanded in recent work (Thompson et al., 2015a,b). We transformed each radiance spectrum L to an *apparent reflectance*ρ, normalizing by solar irradiance F and solar zenith ϕ via:

$$\rho = \frac{\pi L}{F \cos(\phi)} \quad (1)$$

As in Gao et al. (1993) we disregarded coupling between absorption and scattering, relating ρ to the remote sensing reflectance R_{rs} by:

$$R_{rs} = \left(\frac{1}{\pi}\right) \frac{\rho/T_g - \rho_0}{T_d T_u + S(\rho/T_g - \rho_0)} \quad (2)$$

where T_g was the gaseous transmission of the atmosphere, T_u and T_d were upward and downward transmission due to scattering, S was the spherical sky albedo and ρ_0 was the path reflectance due to scattering.

The scattering terms incorporated molecular (Rayleigh) scattering as well as particle scattering due to aerosols. We calculated the scattering coefficients in advance using the 6S code (Vermote et al., 1997; Teillet, 1989; Tanré et al., 1990) with a 20 layer model atmosphere. We used several different aerosol particle combinations spanning a range of optical depths: {0.76, 0.58, 0.44, 0.32, 0.25, 0.18, 0.14, 0.12, 0.03} at

550 nm. At each optical depth, the algorithm assessed four particle models: The canonical rural and marine odels from Shettle (1990), a third option for no aerosols, and a fourth model crafted from equal parts rural and water-soluble particles. This fourth option had no direct precedent in literature but was close to the rural model and better fit the data in this study. We have continued to use this aerosol set without further modification in the subsequent years for delivered reflectance products in all JPL airborne campaigns. Other options, such as the parameterization in the SeaDAS algorithm (Ahmad et al., 2010), could also be used.

We calculated reference transmissions using gas absorption coefficients derived from the Oxford Reference Forward Model (Dudhia, 2014) with the HITRAN 2012 line list (Rothman et al., 2013), and resampled them with the instrument response function. We modeled transmission of gases including H_2O, O_2, CO_2, CH_4, CO, O_3, and N_2O. The gas absorption coefficients depended on pressure elevation and the spatially-variable concentration of H_2O vapor. Consequently we calculated gas transmission values and aerosol coefficients for each of five pressure elevation gridpoints spaced linearly from sea level to the sensor altitude, and 60 candidate column water vapor amounts spaced logarithmically from 0 to 5 cm precipitable water vapor. After these calculations, we stored all wavelength-dependent coefficients needed for Eq. (2) in a 4-dimensional lookup table parameterized by H_2O vapor absorption path, pressure altitude, AOD and aerosol type. At runtime, we retrieved the atmospheric state using characteristics of each TOA spectrum, and then found precise coefficients using bilinear interpolation. Our retrieval first retrieved the pressure altitude using the depth of the oxygen A band, as in Thompson et al. (2015a).

We estimated the aerosol depth and particle model dynamically for each scene by exploiting the presumed reflectance of specific reference surfaces (Guanter et al., 2008). We considered two reference types. First, we flagged dark green vegetation with its high Normalized Difference Vegetation Index (NDVI), and required that it must have a reflectance close to 5% in the 450–500 nm range. Second, we recognized deep water by a low SWIR signal, and required that it must have strong liquid water absorption permitting at most a flat SWIR reflectance due to sunglint. These heuristics defined intervals bounded by the lowest and highest permissible values of ρ, denoted by ψ_{lo} and ψ_{hi} respectively. Our values appear in Table 2, where ϵ was a conservative estimate of measurement noise and ρ(*NIR*) estimated specular sunglint (Hochberg et al., 2011):

$$\rho(NIR) = \inf\{\rho(750), \rho(850), \rho(1050), \rho(1550), \rho(2150)\} \quad (3)$$

We defined the following error function:

$$f(\rho) = \sup \begin{cases} \rho - \psi_{lo} \text{ if } \rho > \psi_{lo} \\ 100\,(\psi_{hi} - \rho_{hi}) \text{ if } \rho < \psi_{hi} \\ 0 \text{ if } \psi_{lo} \le \rho \le \psi_{hi} \end{cases} \quad (4)$$

Values below the lower limit were heavily penalized to prevent non-physical negative reflectances. We applied all errors to relevant pixels of each reference type. We then performed a brute force search over all combinations of AOD and aerosol type, applying Eq. (2) to reference locations and used the sum error over all such pixels to select the best-scoring combination to use for the scene.

The standard aerosol models used in MODTRAN and 6S were derived from Shettle (1990), and included continental, urban, and maritime mixtures. These improved the spectra, with our criterion favoring the continental case 70% dust-like and 29% water-soluble particles. However, we found that a mixture of 50% and 50% better removed vog effects over the entire spectral range including the shortwave infrared. We added this mixture to the library of options available for all flightlines. After searching over all candidate AODs, the 50%/50% model consistently achieved the best scores and AOD consistency across similar flightlines on the same day. Fig. 8 shows an example aerosol retrieval for a line acquired on 17 Jan 2017. The top panel shows retrieved coefficients for Eq. (2) based on our custom aerosol model. The bottom panel shows an example spectrum demonstrating an improvement in retrieved R_{rs} of dark water. This illustrates the dramatic aerosol correction required for flightlines used in these experiments, and the necessity for adaptive aerosol estimation. A subtle residual dip persisted from 650 to 800 nm even after correction. This effect became increasingly prominent close to land, and appeared with other signatures diagnostic of scattered light from nearby terrestrial vegetation. All aerosol effects were calculated using a midlatitude summer atmospheric profile with a relative humidity of approximately 75% at sea level.

We next found the water vapor path using a Continuum Interpolated Band Ratio (CIBR) (Green et al., 1989) estimate of atmospheric absorption features. When the water surface was smooth and water column was clear, there would be very little signal in these wavelengths. However, the estimation was still possible in cases where it mattered most: turbid waters with suspended sediment, or in the presence of sunglint. A linearized nonnegative spectrum fit refined this estimate as in Thompson et al. (2015b). After using these retrievals to find a precise location in the lookup table, Eq. (2) determined R_{rs} above the water surface.

2.2. Glint removal

We next transformed the remote sensing reflectance R_{rs} into the reflectance below the water surface, $R_{rs,0}$, by accounting for sunglint, refraction, and internal reflectance (Lee et al., 1998, 1999). We removed specular solar glint from individual wave facets following methods described in Hochberg et al. (2011). This exploited strong water absorption in Near- and Shortwave Infrared wavelengths. We attributed any nonzero reflectance after atmospheric correction to specular glint, taken to be a uniform additive contribution. We subtracted the reflectance $R_{rs}(NIR)$ at long wavelengths uniformly from the entire spectrum to remove this contamination. Our estimate used the signal level at 1050 nm, or longer where SWIR measurements were available. We then transformed the result to $R_{rs,0}$ using Lee et al. (1998) Eq. 25:

$$R_{rs,0} = \frac{R_{rs} - R_{rs}(NIR)}{1.562(R_{rs} - R_{rs}(NIR)) + 0.518} \quad (5)$$

This empirical relation presumed a spectrally-constant value for the product of internal reflectance between the air/water and the reflective media below with the subsurface directional variation.

2.3. Water property retrieval

Our spectroscopic retrieval of water properties and bottom reflectance could accommodate both AOP and IOP-based models. We will first describe the AOP approach (Maritorena et al., 1994). Following our convention (Table 1) of directional R_{rs} units, we used the convenient assumption that the seafloor was Lambertian, in which case the angular reflectance was related to the Lambertian hemispherical reflectance R_b by a factor of π:

$$\hat{R}_{rs,0} = R_{rs,\infty} + (R_b/\pi - R_{rs,\infty})\, e^{-2KH} \quad (6)$$

Formally speaking the seafloor was not Lambertian, but the assumption supported the ultimate objective to recover relative reflectance signatures for determining seafloor composition. We represented $R_{rs,\infty}$ using the backscatter coefficient b_b. We extrapolated the relationship for the diffuse reflectance of deep water, $R_\infty = b_b/(2K)$ to the angular case as $R_{rs,\infty} = b_b/(2K\pi)$. Due to the simplification of angular independence we caution against a direct interpretation of these terms as the physical backscatter and attenuation, but retrieving them in this fashion on a per-pixel basis proved effective for recovering bottom reflectance shapes. Our second approximation treated the diffuse

Table 1
Notation conventions used in the paper. Following the conventions of atmospheric and aquatic remote sensing communities, we will use irradiance reflectance (ratios of upwelling to downwelling irradiance) for atmospheric quantities, and angular measures (ratios of radiance to downwelling irradiance) for quantities below the water surface.

Symbol	Variable
Γ	Numerator constant used for correction of air/water interface effects
ζ	Denominator constant used for correction of air/water interface effects
η	Atmospheric aerosol mixture type
ρ	apparent reflectance, the ratio of upwelling to downwelling irradiance
ρ_0	Atmospheric path reflectance
ρ_W	Water column path reflectance
$\rho(NIR)$	Near-infrared or shortwave reflectance used to estimate specular sunglint
τ	Atmospheric aerosol optical depth
ϕ	Solar zenith angle
ϕ_v	Viewing zenith angle
Φ_k,Φ_b,Φ_r	Nonnegative mixture coefficients for apparent attenuation, apparent backscatter, and bottom reflectance respectively. All are column vectors with one element per library endmember.
ψ_{lo}	Low extreme of expected TOA reflectances at a specific wavelength
ψ_{hi}	High extreme of expected TOA reflectances at a specific wavelength
b_b	View-dependent apparent backscatter
κ	Attenuation coefficient of (Lee et al., 1999)
D_u^B, D_u^C	Path elongation factors used in HOPE parameterization of (Lee et al., 1999)
F	Solar irradiance
H	Depth of water column (meters)
K	Diffuse attenuation
K_d	View-dependent apparent attenuation
L	Upwelling radiance at the sensor
P_c	Probability of correct benthic type classification
R_W	Diffuse reflectance above the water surface (hemispherical)
R_0	Diffuse reflectance below the water surface (hemispherical)
R_∞	Diffuse reflectance of deep water (hemispherical)
R_{rs}	Remote sensing reflectance above the water surface (directional, per steradian)
$R_{rs,0}$	Remote sensing reflectance below the water surface (directional, per steradian)
$R_{rs,\infty}$	Remote sensing reflectance of deep water (directional, per steradian)
R_b	Benthic reflectance (hemispherical)
S	Spherical sky albedo at the surface
S_W	Spherical albedo of water column at the seafloor
T	Atmospheric transmission
T_d	Downward transmission due to atmospheric scattering
T_u	Upward transmission due to atmospheric scattering
T_g	Transmission due to atmospheric gas absorption
T_W	Water column transmission
U_k,U_b,U_r	Endmember libraries for apparent attenuation, apparent backscatter, and bottom reflectance respectively. All are matrices with one row per instrument channel and one column per endmember.

Table 2
Interval tests defining the aerosol retrieval error. ϵ is a conservative estimate of measurement noise and $\rho(NIR)$ is an estimate of sunglint.

Class	Applies when	Predicted wavelengths (nm)	ψ_{lo}	ψ_{hi}
Dark vegetation	$(\rho(860)-\rho(660))/(\rho(860)+\rho(660))>0.6$	420, 500	$-\epsilon$	$0.05+\epsilon$
Deep water	$\rho(1650)<0.03$ and $\rho(850)<0.05$	750, 850, 1050, 1550, 2150	$\rho_{min}-\epsilon$	$\rho_{min}+\epsilon$

attenuation curves K_d as an "operational K," as described in Maritorena et al. (1994). This was justified for clear waters and near-nadir viewing angles where the attenuation term was fairly stable. Note that b_b, K_d, and R_b were dependent on wavelength and therefore vector-valued. Retrieving depth, this gave $3n+1$ free parameters for only n spectral measurements so in principle the free parameters were underdetermined.

In practice these parameters only spanned a small subspace, so we represented the spectrally-varying values with linear combinations of basis vectors (Klonowski et al., 2007; Hamylton, 2011; Hedley et al., 2004; Dekker et al., 2011; Petit et al., 2017). We posited linear mixing models in which K_d, b_b, and R_b each lay in their own subspaces defined by matrices of library endmember spectra U combined according to nonnegative mixing coefficients Φ. Since clear water had its own attenuation, we enforced minimum values with an additive offset spectrum u_k. The linear subspace captured the additive portion above this floor. A similar spectrum u_b set a floor value for b_b. Subscripts distinguished the three mixtures:

$$K_d = u_k + U_k\Phi_k, \quad b_b = u_b + U_b\Phi_b, \quad R_b = U_r\Phi_r \tag{7}$$

The complete model used nonnegative Mixing coefficients:

$$\widehat{R}_{rs,0} = \frac{b_b}{2K_d\pi} + \left(\frac{R_b}{\pi} - \frac{b_b}{2K_d\pi}\right) e^{-2HK_d} \quad \text{for } \{H, \Phi_b, \Phi_k, \Phi_r\} \geq 0 \tag{8}$$

Free parameters consisted of the scalar H and the vector-valued Φ_b, Φ_k and Φ_r. The columns of each U contained the linear endmembers (Keshava and Mustard, 2002), combinations of which represented retrieved spectral quantities. This linear model uniquely specified shapes of K_d and b_b, but not necessarily their magnitudes. Consider a depth perturbation by a factor δ; a valid solution leaving $R_{rs,0}$ unchanged would be:

$$H' = (\delta)\,H, \quad K_d' = (1/\delta)\,K_d, \quad b_b' = (1/\delta)\,b_b, \quad R_b' = R_b \tag{9}$$

This invariance decoupled H from R_b under an inversely proportional change to backscatter and diffusion. Consequently, the linear model used relative radiometry to recover R_b based on spectral shapes, providing resilience against magnitude errors in K_d and b_b for the ultimate objective of estimating R_b.

We drew endmembers from spectral libraries, with larger library subsets improving representational accuracy at the cost of more free parameters. Endmembers for b_b, K_d came from simulations by the Hydrolight radiative transfer code (Mobley and Sundman, 2001) for different water constituents. R_b endmembers came from a database of reflectance spectra acquired by in-situ field teams or from historical observations of similar environments (Hochberg et al., 2003). We selected endmember subsets using the Sequential Maximum Angle Convex Cone (SMACC) method (Gruninger et al., 2004). This began with U as a one-column matrix containing a single endmember: the spectrum with the highest albedo. It then sequentially added columns to U by appending the library spectrum with the largest orthogonal projection onto the subspace formed by the existing set. The process grew a high-volume subspace within the original space spanned by all library spectra. Reconstruction error indicated the asymptote beyond which additional endmembers did not significantly improve the representation fidelity. We performed this process for U_b, U_k, and U_r. Fig. 2 shows the reduction in mean RMSE reconstruction error for the entire library, as a function of the size of the endmember subset. These curves suggested that the intrinsic dimensionality of the subspace of physical conditions was indeed much smaller than the number of measured channels. Inflection points in the curves indicated effective cutoff points - just two endmembers captured the variability in backscatter, while K_d required 5–6 (Fig. 3). The bottom reflectance was typically more complex and required 8–15 endmembers or more. Fig. 3 shows the endmember spectra (columns of each U) used in a typical analysis. We illustrate the complete catalog using light gray and the selected endmembers in black. Extra endmembers did not harm the retrieval results so it would have been safe to augment the automated results with hand-selected spectra.

While a complete library was preferable, an incomplete library could still reproduce some spectral shapes not present in the original set. Most prior algorithms from the literature precalculate intermediate

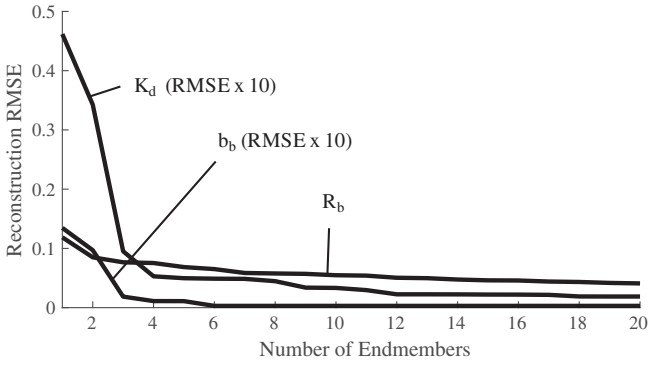

Fig. 2. Larger endmember libraries enabled better reconstruction accuracy at the cost of additional free parameters. Curves show mean RMSE reconstruction error for the libraries of simulated b_b and K_d, as well as the R_b library compiled from field spectra.

values using a finite number of spectrum "options" and then select the best. In contrast, we estimated the continuous-valued mixture fractions simultaneously for all library spectra, for each spectrum. For this reason, the algorithm could converge to a linear combination of library absorption features to produce a novel spectral shape. Fig. 2 portrays this graphically, showing minimal RMSE benefit beyond 15–20 endmembers.

We used Bayesian priors to discourage radical departures from physically-plausible expected values. They also served as a stabilizing influence and a rigorous way to incorporate complementary information if available. The conditional probability of a state vector given measurements decomposed by Bayes' rule into data likelihood and prior terms:

$$P(H, U_b, U_k, U_r \mid \hat{R}_{rs,0}) \propto P(\hat{R}_{rs,0} \mid H, U_b, U_k, U_r) P(H, U_b, U_k, U_r) \quad (10)$$

Finding the state vector to maximize this probability amounted to Bayesian Maximum a Posteriori (MAP) estimation (Rodgers, 2000; Lewis et al., 2012). We used a simple model where the prior quantities were conditionally independent and the distribution factorized:

$$P(H, U_b, U_k, U_r \mid \hat{R}_{rs,0}) \propto P(\hat{R}_{rs,0} \mid H, U_b, U_k, U_r) P(H)\, P(U_b)\, P(U_k)\, P(U_r) \quad (11)$$

It was sufficient to use Gaussian prior distributions defined by a standard deviation σ and expected value μ. The σ weighted each free parameter according to its expected variability, while the μ defined the mean of the prior. These could be set directly from field data or fit using hyperparameter learning methods (Bishop, 2006), but we found it was not critical to provide statistically perfect prior distributions since they amounted to a "soft" regularizer and enough measurement evidence could overcome them. Absent measurements we opted for lenient priors with large σ, and left the depth prior essentially unconstrained unless there was high-quality bathymetry. We found that we could adjust the other priors based on selected field measurements and prior knowledge and successfully apply the same uniform settings across all the scenes in our study. The Gaussian form was:

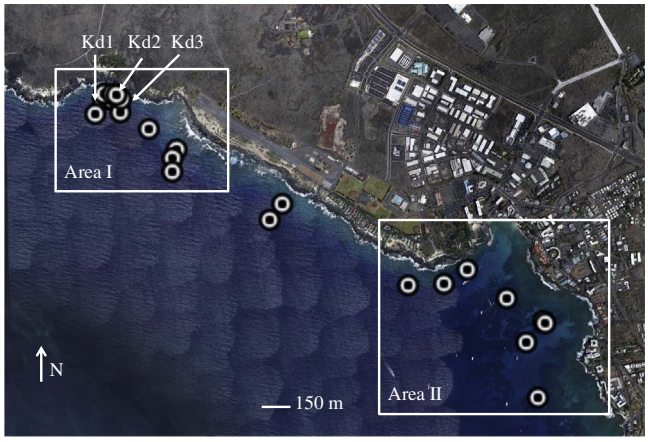

Fig. 4. Evaluation sites in the Kona region. Dots indicate locations where in-situ K_d or area-averaged benthic reflectance is available. Arrows indicate the first three Kd castings, illustrated in Fig. 4. Graphic courtesy Google Earth, Google, Inc.

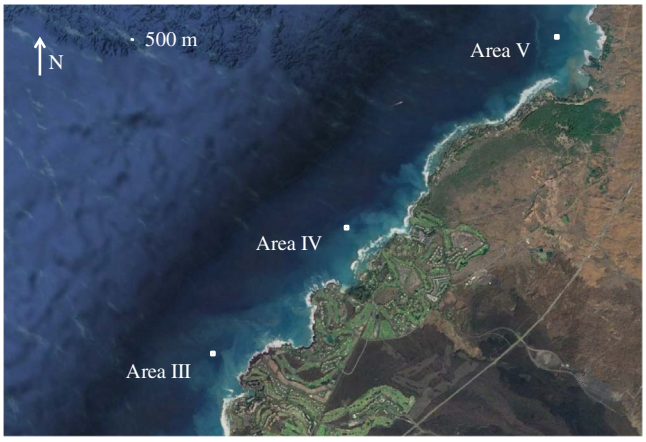

Fig. 5. Bathymetry evaluation sites. Graphic courtesy Google Earth, Google, Inc.

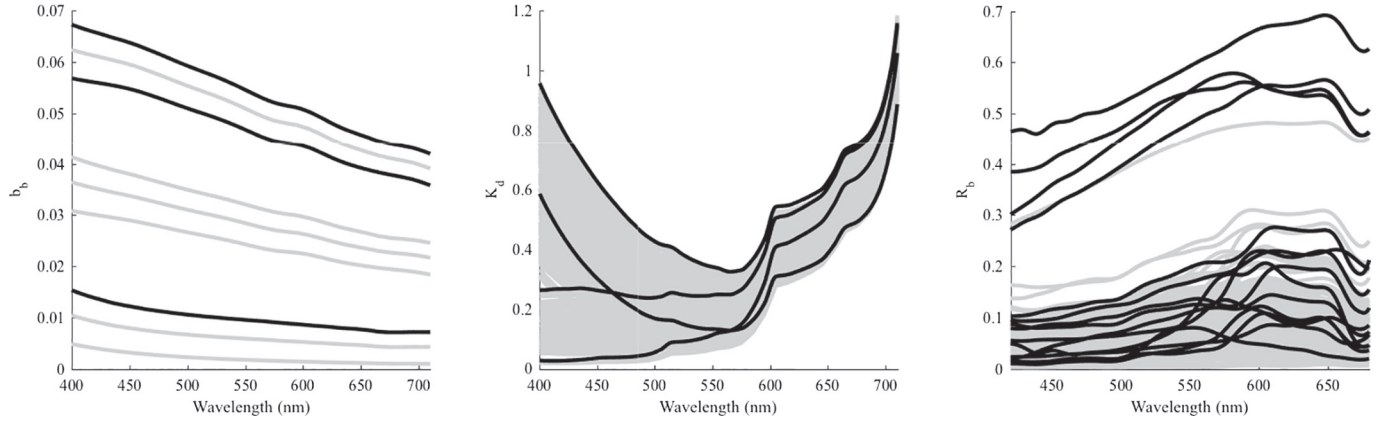

Fig. 3. Example endmembers used in nonnegative mixing model. Gray spectra show the entire library. Black spectra show selected endmembers including offsets for K_d and b_b quantities. Left: backscatter b_b. Center: diffuse downward attenuation K_d. Right: R_b.

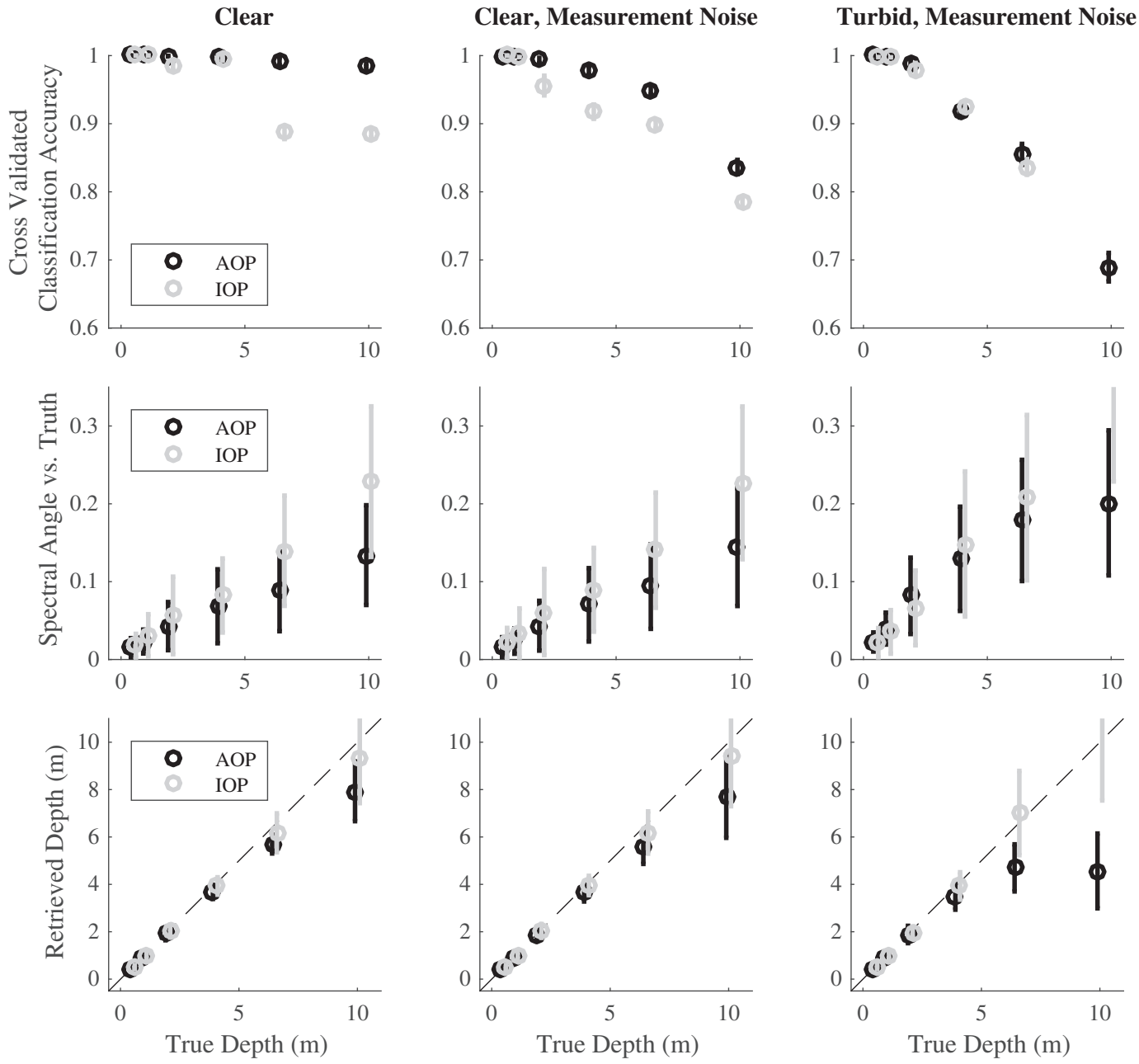

Fig. 6. Classification, spectral angle, and depth retrieval accuracy for both models for noise free, noisy, and turbid noisy observations. Better matches are associated with high classification accuracies and small spectral angles. Accurate depth retrievals lie on the diagonal 1:1 line. Error bars show standard deviations for 5000 trials.

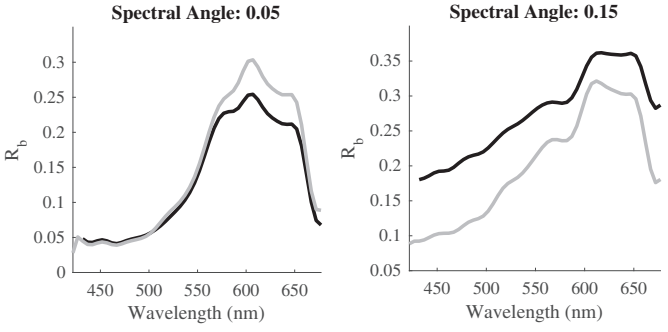

Fig. 7. Example spectra for coral (left) and algae (right) illustrate different spectral angle scores. A larger spectral angle indicates a poor match, but may still preserve spectral absorption features that provide interpretability.

$$P(H, U_b, U_k, U_r \mid \hat{R}_{rs,0}) \propto \left[\prod_{\lambda} \exp\left(-\frac{(\hat{R}_{rs,0}-\mu_R)^2}{\sigma_R^2}\right)\right] \exp\left(-\frac{(H-\mu_H)^2}{\sigma_H^2}\right) \exp\left(-\frac{(K_{d590}-\mu_{Kd590})^2}{\sigma_{Kd590}^2}\right) \exp\left(-\frac{(K_{d450}-\mu_{Kd450})^2}{\sigma_{Kd450}^2}\right) \exp\left(-\frac{(b_{b590}-\mu_{bb590})^2}{\sigma_{bb590}^2}\right) \quad (12)$$

Here σ_R was the standard deviation of the reflectance measurement noise, calculated based on deviation from nonparametrically smoothed profile of dark NIR channels (Wasserman, 2007). Variables μ_H and σ_H were the mean and standard deviation of a prior over depth H. Other subscripts specified priors on specific wavelengths. For example, μ_{Kd590} and σ_{Kd590} were the prior mean and standard deviation of K_d at 590 nm. Thus, Eq. (12) had five terms: a data likelihood combined with priors over depth, b_b at 590 nm, K_d at 450 nm, and K_d at 590 nm. We selected

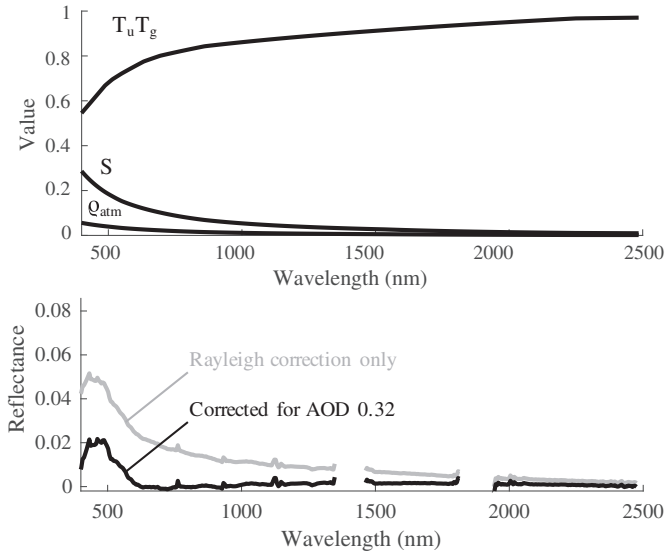

Fig. 8. Aerosol retrieval for a line acquired on 17 Jan 2017. Top panel: Retrieved coefficients based on Eq. (2), using the aerosol model described int the text. Bottom panel: Example spectrum demonstrating an improvement in retrieved R_{rs} of dark water. This illustrates the dramatic aerosol correction required for flightlines used in these experiments.

the specific wavelengths of these priors to constrain both the magnitude and shape of the AOPs. Since most standard optimizers minimized an error function, we used the negative logarithm resulting in a cost f_{AOP} that comprised additive squared error terms:

$$f_{AOP} = \left[\sum_{\lambda} \frac{(\hat{R}_{rs,0} - R_{rs,0})^2}{\sigma_R^2}\right] + \frac{(H-\mu_H)^2}{\sigma_H^2} + \frac{(K_{d590} - \mu_{Kd590})^2}{\sigma_{Kd590}^2} + \frac{(K_{d450} - \mu_{Kd450})^2}{\sigma_{Kd450}^2} + \frac{(b_{b590} - \mu_{bb590})^2}{\sigma_{bb590}^2} \quad (13)$$

Our retrieval first set the state vector to a random initial guess and then applied Levenberg-Maquardt gradient descent (More, 1978; Garbow et al., 1980) to minimize Eq. (13). We incorporated the nonnegativity constraints directly in the Levenberg-Maquardt problem definition.

The IOP-based model used R_b linear mixture coefficients along with the scalar HOPE parameters of Lee et al. (1999), which use a path elongation term to capture view dependence of R_{rs}. The analogous cost function f_{IOP} used prior means μ and standard deviations σ:

$$f_{IOP} = \left[\sum_{\lambda} \frac{(\hat{R}_{rs,0} - R_{rs,0})^2}{\sigma_R^2}\right] + \frac{(H-\mu_H)^2}{\sigma_H^2} + \frac{(P-\mu_P)^2}{\sigma_P^2} + \frac{(X-\mu_X)^2}{\sigma_X^2} + \frac{(G-\mu_G)^2}{\sigma_G^2} \quad (14)$$

The optimization was otherwise identical, with nonnegativity constraints incorporated into the Levenberg-Maquardt problem definition.

2.4. Simulation method

We used simulations to demonstrate the correctness of the retrieval approach and compare performance of AOP and IOP versions under different conditions. We defined a virtual reef of random measurements, each based on pairs of library spectra of coral, sand, and algae spectra observed at nadir viewing angle and 25° solar zenith. We mixed library spectra randomly but ensured one constituent dominated above a 90% areal coverage fraction. That component defined the class of the R_b spectrum. We then simulated water columns for clear and turbid simulations using the Hydrolight radiative transfer code (Mobley and Sundman, 2001). A "clear water" case used a Chlorophyll concentration of 0.1 mg m^{-3}, suspended sand of 0.1 g m^{-3}, and a CDOM absorption coefficient of 0.05 at 400 nm. The "turbid" case used a Chlorophyll concentration of 0.1 mg m^{-3}, suspended sand of 0.2 g m^{-3}, and a CDOM absorption coefficient of 0.11. All priors were set to uninformed values (extremely large σ). We applied both IOP and AOP parameterizations, initializing the IOP version according to heuristics from Lee et al. (1999) and initializing the AOP version to uniform coefficients. We assessed performance with and without measurement noise.

Table 3
Atmospheric correction results for flight days in the CAO Hawaii campaign. Water: The number of water pixels used in aerosol estimation. Veg: The number of dark vegetation pixels used in aerosol estimation. Vis: estimated visibility in kilometers. Error: mean improvement in the reflectance error score (Eq. (4)), as a fraction of that incurred by default atmosphere assumptions.

Date	# Water	# Veg	Vis (km)	Error
20160106	3.8E+07	1.5E+07	80.8	0.423
20160111	9.2E+06	1.9E+04	9.0	0.284
20160117	3.1E+07	8.8E+05	16.6	0.185
20160119	4.4E+07	3.5E+06	16.2	0.233
20160122	1.1E+08	1.9E+06	13.0	0.260
20160123	1.5E+07	8.7E+05	15.0	0.056
20160126	6.4E+06	3.0E+06	25.0	0.199
20160127	4.3E+06	6.9E+05	300.0	0.415

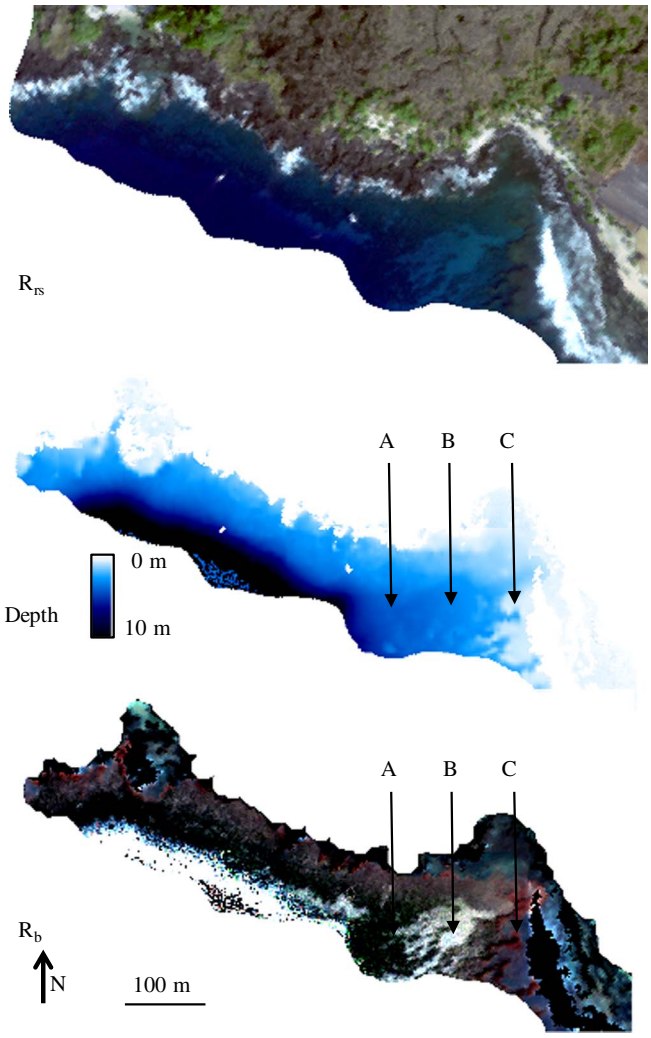

Fig. 9. Site I map products. Top panel: Remote sensing reflectance. Middle panel: Retrieved depth (with a strong prior based on SHOALS LIDAR). Spectra A, B, and C correspond to representative depths referenced in Fig. 10. Bottom panel: Retrieved R_b indicating diverse surface reflectances.

The noisy case perturbed the R_{rs} by a white Gaussian distribution appropriate for the CAO instrument. We estimated noise with a non-parametric approach (Brown et al., 2007) based on the differences between neighboring channels of the spectrally-flat near infrared region. It revealed a standard deviation of 0.0002 for typical scenes.

We applied this procedure over 5000 trials at varying depths, calculating two metrics to score R_b retrieval accuracy. The first was a spectral angle $SA(\hat{R}_b, R_b)$ defined by the dot product between the retrieved and actual R_b vectors:

$$SA(\hat{R}_b, R_b) = \cos^{-1}\left(\frac{\hat{R}_b^T \hat{R}_b}{|\hat{R}_b|_2 \ |R_b|_2}\right) \quad (15)$$

This quantified the match between spectrum shapes (Yuhas et al., 1992). We also used a task-specific score, the accuracy P_c of a supervised classifier trained to categorize benthic coverage type. Here P_c represented the total probability of a correct class assignment (Stehman, 1997), given as $P_c = p_{coral} + p_{algae} + p_{sand}$ where p_{coral}, p_{algae}, and p_{sand} represented the probabilities that a spectrum was of the designated class *and* correctly classified. The total score would be unity for a perfect classifier. We applied a principal component reduction to 20 dimensions followed by Linear Discriminant Analysis (Hochberg et al., 2003). This regularly achieved above 99% accuracy, outperforming alternative classifiers like decision forests (Breiman, 2001) for this dataset size. We evaluated performance with held-out fractions using 5-fold cross validation.

2.5. Field experiment method

Airborne remote sensing data were acquired in January 2016, coinciding with our field campaign, using the Carnegie Airborne Observatory, or CAO (Asner et al., 2012), which includes a high-fidelity Visible-to-Shortwave Infrared (VSWIR) imaging spectrometer. We collected the VSWIR image data over the two study areas from an altitudes of 1000 m and 2000 m above ground level (AGL) at an average flight speed of 55–60 m s^{-1}. The CAO VSWIR spectrometer measures spectral radiance in 427 channels spanning the 380–2510 nm wavelength range in 5 nm increments (full-width at half-maximum). The VSWIR has a 34° field of view and an instantaneous field of view of 1 mrad. At 1000 m and 2000 m AGL respectively, the VSWIR data collection provided 1.0 m and 2.0 m ground sampling distance, or pixel size. The VSWIR data were radiometrically corrected from raw DN values to radiance (W m^{-2} sr^{-1} nm^{-1}) using a flat field correction, radiometric calibration coefficients and spectral calibration data collected in the Carnegie Institution's airborne science laboratory.

Precise geo-orthorectification of the VSWIR data was achieved by fusion with the CAO Light Detection and Ranging (LIDAR) system. The LIDAR has a beam divergence set to 0.5 mrad, and was operated at 200 kHz with 17° scan half-angle from nadir, providing swath coverage similar to the VSWIR spectrometer. The LIDAR point density was two laser shots m^{-2}, or 2–8 shots per VSWIR pixel. The LIDAR data were combined with an embedded high-resolution Global Positioning System-Inertial Measurement Unit (GPS-IMU) data to produce a cloud of georeferenced point data. Digital sea and land surface models (DSM) were calculated using the method described in Asner et al. (2007). The standardized GPS pulse-per-second measurement was used to precisely co-locate VSWIR spectral imagery to the LIDAR data using the technique detailed by Asner et al. (2012). The VSWIR imagery was then orthorectified to the LIDAR DSM. We analyzed all radiance data using standard atmospheric correction methods, using both deep water and dark vegetation features as in Table 2.

We selected two specific study areas near the Kona region (Fig. 4) for in-depth study. The two areas were each overflown three times on 17 January 2016 at 19:10 h, 19:21 h, and 19:30 h UTC - approximately 10:30 h local time. Meanwhile, in-situ survey teams deployed a Biospherical Instruments, Inc. PRR-800 Profiling Reflectance Radiometer (Biospherical Instruments Inc., 2011) at several geotagged sites to profile upwelling radiance and downwelling irradiance at multiple depths and wavelengths. This permitted direct calculation of the diffuse attenuation and backscatter. Additionally, area-averaged bottom reflectance spectra were acquired at two geo-tagged locations over an 8 m quadrat. Atmospheric conditions were observed from the field and from the air to be sub-optimal, with heavy vog (volcanic smog) causing

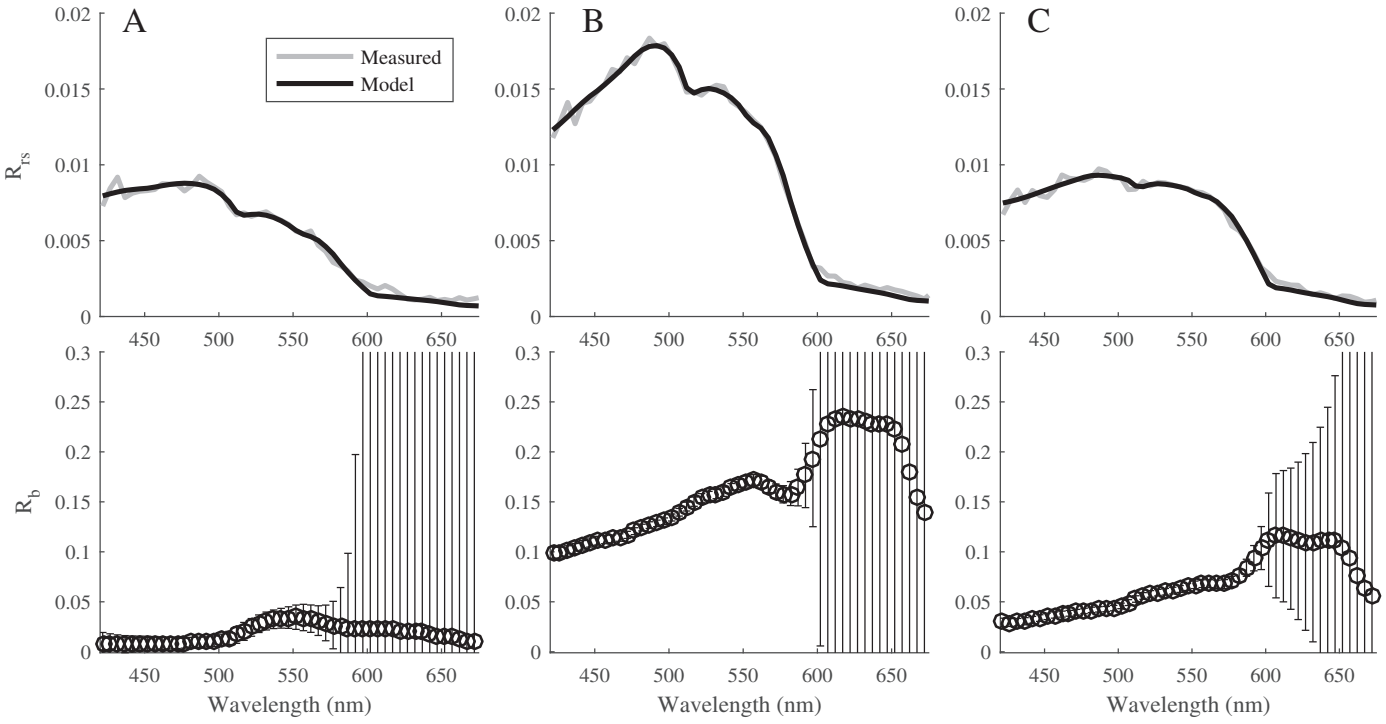

Fig. 10. Typical R_{rs}, model R_{rs}, and R_b spectra. A: example retrieval for 13.6 m depth. B: example retrieval at 9.4 m depth. C: example retrieval at 7.7 m depth. Error bars indicate noise-equivalent (1σ) changes in R_b.

significantly reduced visibility over the study site. To provide an independent dataset for depth validation, a second flightline over the Hawaii coast acquired VSWIR airborne data on 27 January 2016 at 20:49 h UTC under clear-sky conditions. We reprojected this dataset, and the original vog-contaminated flightlines used for reflectance retrievals, to bathymetric LIDAR data acquired in 2001 from the SHOALS instrument (Wozencraft and Lillycrop, 2002). We studied three subregions that had reasonable spatial separation, good depth contrast, good overlap between the two instruments, and distinctive depth features (Fig. 5). Together, the five sites (labeled I–V) constituted two separate and distinct experiments isolating performance of the benthic reflectance and depth retrieval algorithms.

We applied our AOD retrieval method, setting priors over K_d based on 11 in-situ castings. These indicated clear water, with K_d values less than 0.05 at 450 nm. For the depth retrieval experiment, we set very lenient priors over depth, amounting to essentially no constraint. For the bottom reflectance retrieval, we set priors over depth directly using LIDAR bathymetry, with a mean equal to the known depth at each pixel and a tight standard deviation of 0.01. This caused the depth to be effectively fixed at the known value.

The CAO dataset, combined with benthic LIDAR and in-situ observations, provided overlapping information to bound the accuracy of the spectroscopic analysis chain. We analyzed the atmospheric correction for agreement with the visual observations of atmospheric conditions in pilot logs and ground observations of haze and vog. The spectra themselves were an independent standard; known properties of surface reflectance (the standards of Table 2) score the aerosol model's success in removing scattering across all wavelengths. For the benthic reflectance experiment, three different in-water sampling locations overlapped with the airborne datasets providing multiple comparisons across different overflights. We co-registered the in-water and retrieved measurements to compare accuracy directly. For the depth retrieval experiment, the airborne LIDAR bathymetry data served as a benchmark standard.

3. Results

3.1. Simulation results

The simulations showed the performance of both AOP and IOP models in different conditions. Fig. 6 (top row) shows classification accuracy for noise free, clear, and turbid cases. Both showed a smooth loss of accuracy as depth increased. The loss of accuracy was faster for higher levels of suspended particles. In the difficult conditions the degradation accelerated significantly beyond approximately 6–8 m depth and left very little information beyond 10 m. Such findings corroborated previous studies with comparable instruments that found retrievals degrade significantly beyond this depth, e.g. Zoffoli et al. (2014). Nevertheless, for clear-water conditions and shallow turbid environments, accuracies above 75% could be operationally useful for mapping benthic coverage type. The high sensitivity to suspended particles suggested that such campaigns' success would hinge on local water conditions.

Fig. 6 (middle row) shows the results for spectral shape matching. Interestingly the AOP and IOP versions showed some minor divergence in performance, with the AOP version providing better accuracy in both clear and turbid water. Note that the spectral angle scores for turbid water decayed much more rapidly than the classification scores. To demonstrate how this could occur, Fig. 7 shows two examples from simulation. The dark lines in each panel portray the actual spectrum and the gray lines show the retrieved estimate. The left panel's spectral angle of 0.05 is a “success” case typical of shallow and clear water in which slopes, magnitudes, and fine spectral features all aligned. The left panel with a spectral angle of 0.15 shows discrepancies in the slopes and vertical offsets of the two spectra. However, the finer spectral features and profiles were preserved, underscoring that poor spectral matches did not necessarily translate to a loss of interpretability or classification performance. Note that the spectral angle scores for turbid water decayed much more rapidly than the classification scores.

Finally, Fig. 6 (bottom row) shows the accuracy of retrieved depth for each model. The IOP approach tracked the true depth better than the AOP method, possibly due to the indeterminacy noted above in the AOP's retrieved magnitude for K_d, b_b, and depth. Overall, the IOP achieved superior depth retrieval while the AOP provided more accurate R_b spectra. Naturally this simplified experiment in a controlled setting could not perfectly predict performance in field conditions, but it suggested how the different parameterizations affected our algorithm's ability to invert the full radiative transfer model.

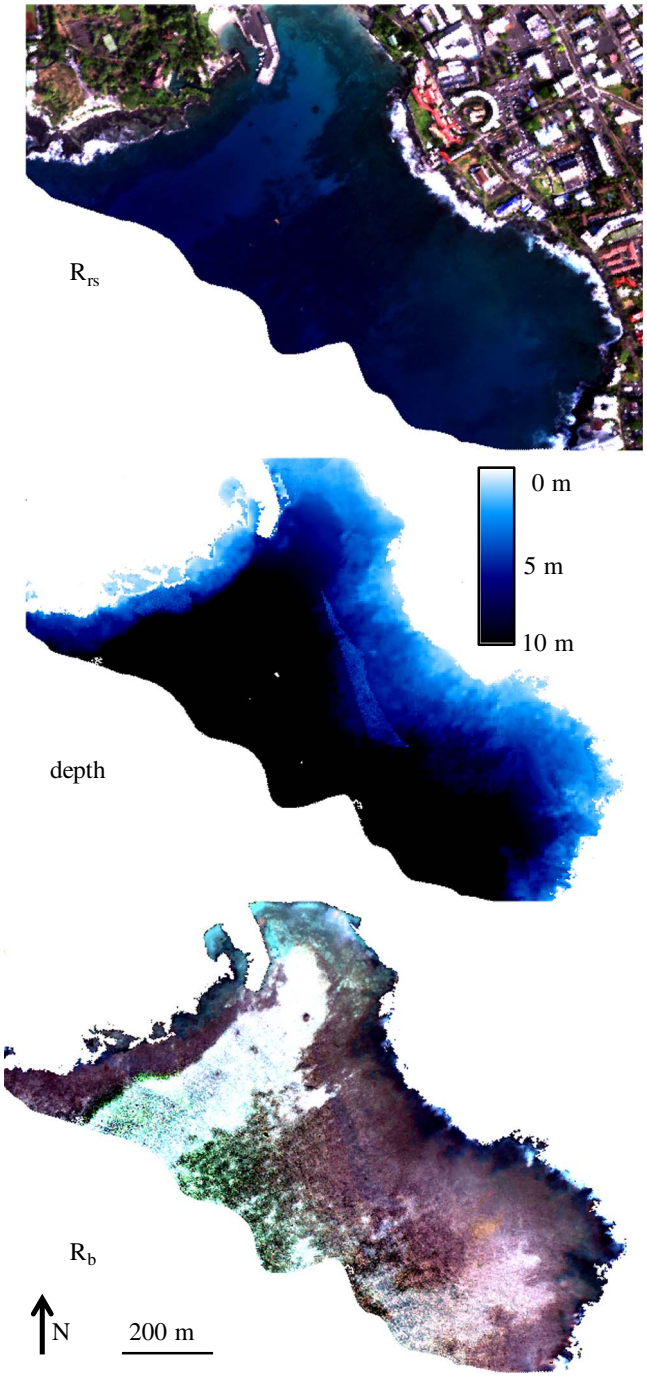

Fig. 11. Site II map products. Top panel: Remote sensing reflectance. Middle panel: Retrieved depth (with a strong prior based on SHOALS LIDAR). Bottom panel: Retrieved R_b.

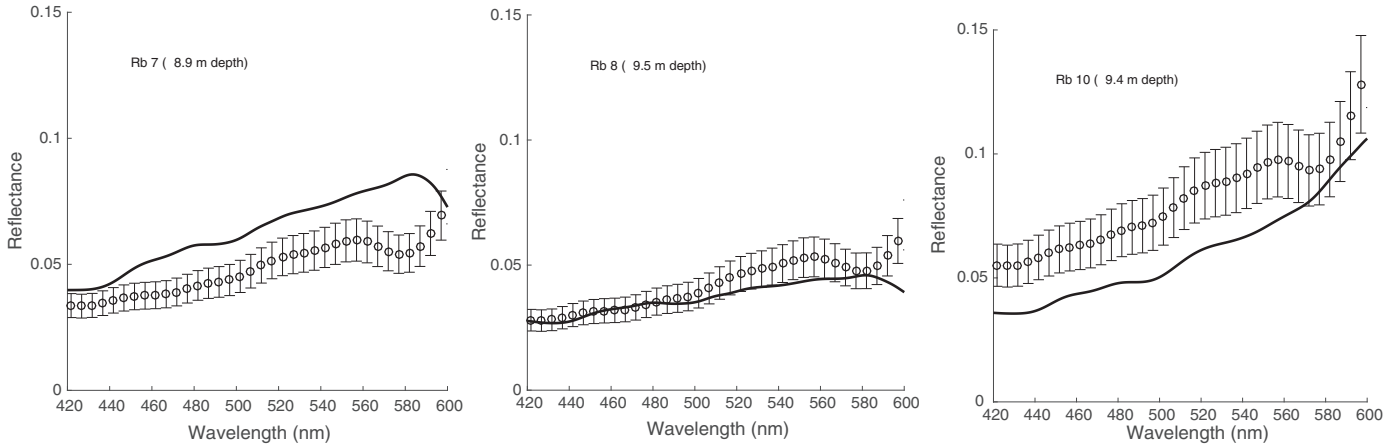

Fig. 12. Comparison of remote and *in situ* measurements of the average R_b spectrum over a 10 m^2 area. Thick lines indicate the *in situ* data. Error bars show the 95% confidence for remote measurement based on root-sum-squared combination of R_{rs} measurement noise and spectrum variance within each 10×10 averaging zone. This conservative error estimate excludes errors in water column constituents. Error in the in-situ measurement is not characterized.

3.2. Field experiment results

Table 3 summarizes atmospheric correction results for the 59 flightlines in the CAO Hawaii campaign. The second and third columns show the number of water and vegetation pixels available for aerosol estimation. The fourth column reports average visibility in kilometers across all flightlines as retrieved by the R_{rs} retrieval algorithm. The "Error" column expresses the mean improvement in the reflectance error score after applying aerosol correction (Eq. (4)), expressed as a fraction of the error incurred by the default atmosphere with Rayleigh scattering only.

Fig. 9 shows the R_{rs}, Depth, and R_b maps for area I. Foam and land pixels were filtered from the retrieval results using NIR reflectance thresholds. Arrows indicate three representative locations at different depths: (A) 13.6 m, (B) 9.4 m, and (c) 7.7 m. Their spectra appear in Fig. 10. The top row of Fig. 10 shows the measured and modeled R_{rs} at each location, indicating a good model fit in all cases. The bottom row shows the corresponding retrieved R_b spectra. We formed 1σ error bars by translating R_{rs} measurement noise into the noise-equivalent R_b assuming the depth and water properties are correct. This was an optimistic lower bound on R_b error. Our measurement noise estimate used the observed R_{rs} in smooth, dark NIR channels as described above. The R_b estimate in long wavelengths was most accurate for shallow water, and degraded quickly beyond 10 m. The retrievals revealed characteristic signatures of algae and coral, such as absorption features at 540 nm and 590 nm respectively. Fig. 11 shows similar R_{rs}, Depth, and R_b maps for Area II. The benthic reflectance map shows scene content that is broadly consistent with Area I. It contains shallow near-shore area dominated by algae, trending to a mixture of sand and reef at deeper locations.

Next, Fig. 12 compares the retrieved area-averaged benthic reflectance spectra at the in-situ sampling locations. Here, errorbars indicate the full extent of the data over three flightlines that cover the area. Several caveats apply to this comparison. First, in order to match the *in situ* acquisition process, these spectra represent wide-area averages over 10 × 10 m windows. This spatial averaging smoothed any fine spectral features. Additionally, there was also an uncharacterized error associated with the *in situ* spectroscopic reflectance, a difficult measurement from a hand-held underwater instrument. Finally, both *in situ* and remote area averages lay at the edge of a deep underwater ridge. Since the precise localization underwater was challenging, natural error and variability might yield significant differences in the resulting optical and benthic properties. These caveats aside, the overall magnitude and slope of the two measurements matched to within 1–2% of absolute reflectance (slightly more in the brightest case), providing a check that the reflectances are reasonable matches to ground reference data.

Fig. 13 shows the K_d retrieval for a representative subset of the first three castings, with locations illustrated in Fig. 4. The tight agreement here was expected, since the K_d values were strongly

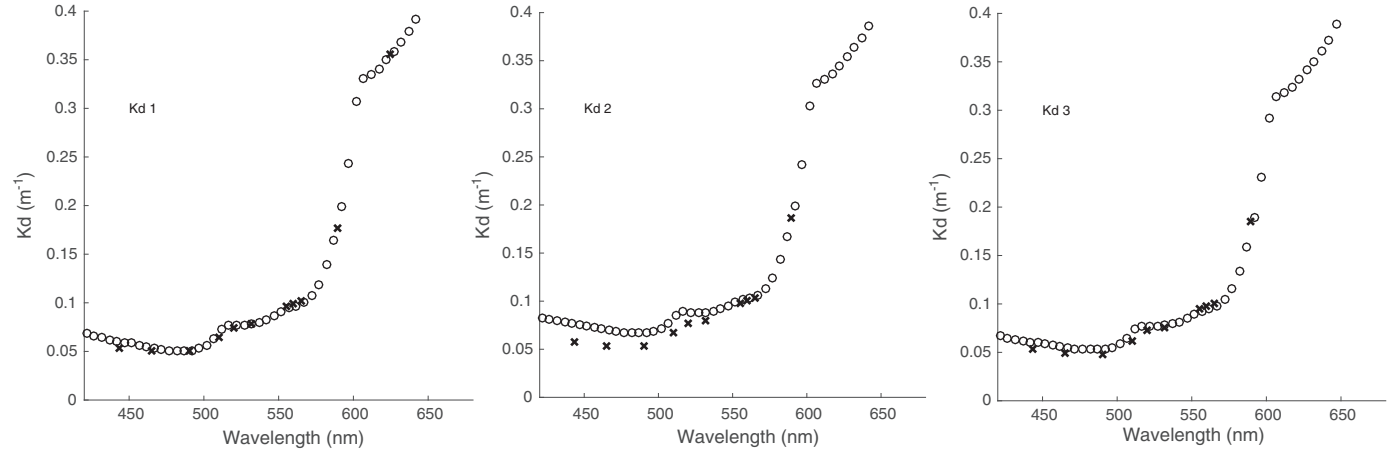

Fig. 13. Comparison of remote and *in situ* measurements of K_d. The dashed line indicates a slope of unity. The first three *in situ* measurement sites appear as dark 'x' symbols. Remote retrievals are averages of 2 scenes for the center and right panels, where multiple overpasses were available.

constrained by the priors from *in situ* measurements. Nevertheless, the result provided confidence that the retrieval incorporated this soft constraint and produced an explanation consistent with all available information.

Fig. 14 shows the results of the depth retrieval experiment, with different panels for bathymetric LIDAR, spectroscopic depth retrievals, and scatterplot comparisons at each of three sites. Here, depth was unconstrained and the variability indicates the accuracy in *tabula rasa* retrievals with fully uninformed priors. In the scatterplots the thick black line indicates a slope of unity. The shape and position of depth features were similar for both instruments. The scatterplots indicate a good correlation between the two depth retrieval methodologies, with a scatter of approximately 1–2 m in shallow water. This could have been related to surface effects or inteference due to breaking waves, foam and other interference near shore. This scatter and discrepancy generally increased at greater depths, consistent with intuition and our simulation results.

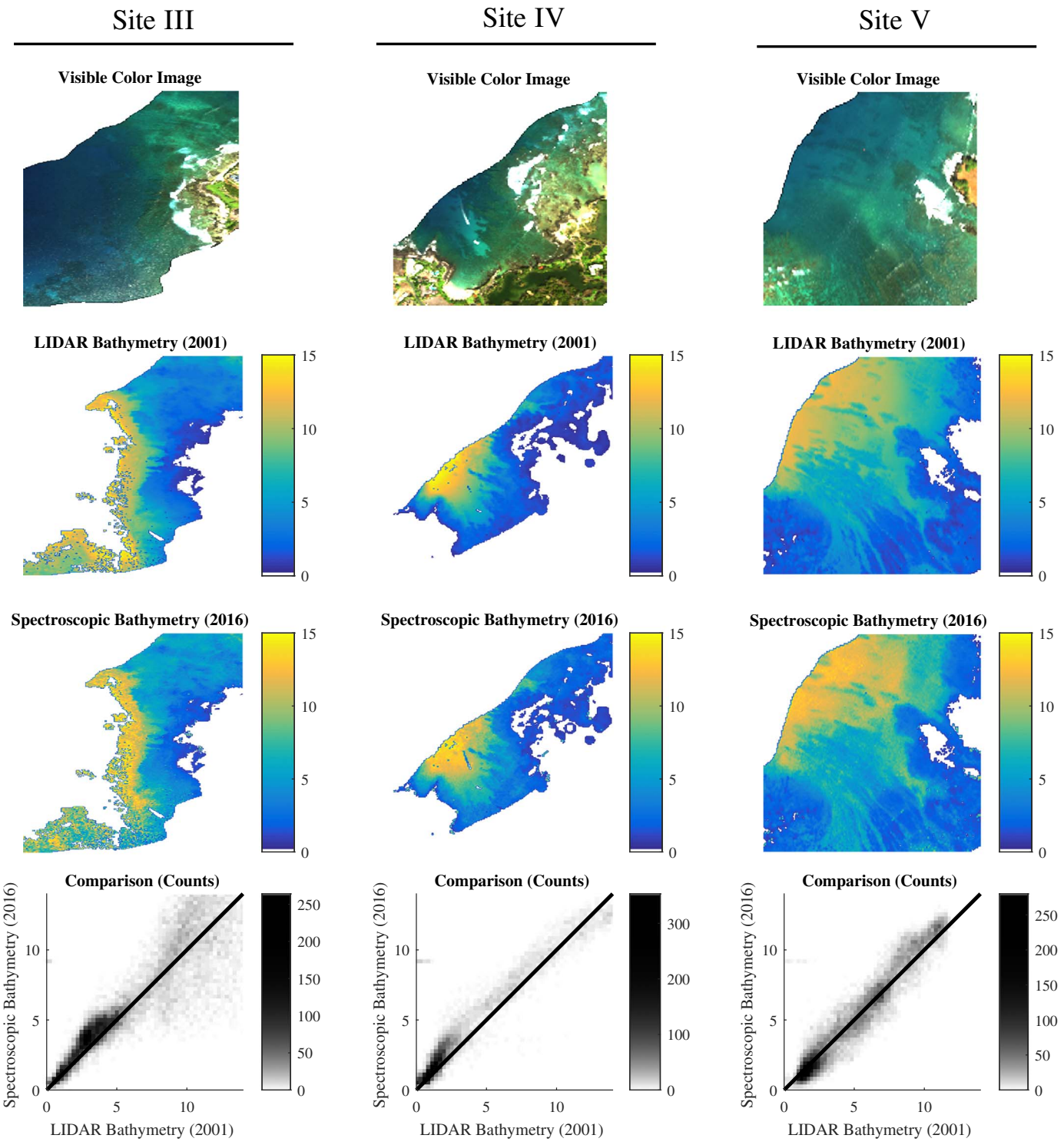

Fig. 14. Comparison of depth retrieval using LIDAR and spectroscopy.

4. Discussion and conclusion

These field experiments demonstrate wide-area mapping of R_b at high spatial and spectral resolution, in agreement with correlated *in situ* and remote measurements. They include the complete analysis chain from radiance at the sensor to an estimate of bottom reflectance for determining the condition of shallow-water ecosystems. Fundamentally, we demonstrate a Bayesian retrieval methodology that permits fast but principled synthesis of prior knowledge and measurement data for application across wide areas with varied ancillary measurements. Statistical priors permit a stable retrieval of reflectance mixture coefficients and optical properties, even when initialized randomly. Other notable aspects include the use of in-scene reflectance heuristics to estimate atmospheric aerosols, and water column models based on linear mixtures of bottom reflectance and Apparent Optical Property components that are simple to measure *in situ*. Given the very challenging atmospheric conditions of the CAO overflights, the results for depth and R_b compare reasonably with *in situ* measurements. The *in situ* reflectance consists of wide area averages acquired with some uncertainty, and consequently does not alone prove or disprove the ability to retrieve fine-scale spectral shapes. However, single-pixel spectra of Fig. 10 do show more distinctive shapes, and the simulations show the retrieval accuracy is comparable to other techniques in current use. One interesting new finding is that, in simulation at least, perfect depth retrieval is not a prerequisite for accurate retrieval of R_b. When in ancillary data is not available, the AOP parameterization leaves some indeterminacy in the depth/AOP magnitudes but still manages to accurately retrieve R_b using spectral shape information.

Both atmospheric and water column conditions can complicate the retrieval. Prior work has recognized the challenge of residual atmospheric effects and glint, including Goodman et al. (2008) and Brando et al. (2009); they affect both AOP and IOP formulations. Heavy aerosol loading was a particular challenge for this field campaign. Certainly, the extreme conditions attempted here, with volcanic fog and estimated Aerosol Optical Thickness from 0.32 to 0.44, push the frontier of feasible retrieval scenarios. The simulations also underscore the importance of water column clarity for effective classification, particularly at depth. This appears at least as important as atmospheric conditions, and suggests that the fundamental challenge for wide area mapping may simply be catching the rare instance where both skies and water are favorable. Orbital sensors providing regular repeat coverage may be the best option to achieve this in the future.

The technique is suited to airborne imaging spectrometers such as PRISM (Mouroulis et al., 2008) and future orbital imaging spectrometer missions (Mouroulis et al., 2016). The AOP approach is one of many different options for the water column model, each with unique advantages and disadvantages. However, the general premise of leveraging R_b library mixtures to reduce the number of free parameters could apply to any water column model. Our formulation can incorporate prior knowledge in a rigorous statistical fashion through Bayesian priors that incorporate the unique measurement certainty of each deployed instrument.

Future work will continue refining the approach. A natural extension would be to permit retrieval of spectra that are not strict linear combinations of library R_b endmembers. A library of 5–10 endmembers should already provide significant flexibility for modeling unusual spectral shapes. However, it is possible — particularly for very high SNR instruments — that subtle unanticipated shifts in absorption peak, slope or position of certain features would not be captured. A possible solution would be to begin with an initial retrieval using the standard approach above, obtain depth and water column properties, and then re-derive R_b independently for each wavelength using the algebraic relationship in Eq. (6).

Another natural extension would be to interpret the retrieved library mixing fractions directly as areal mixtures to perform a bottom cover type classification, as in recent work by Petit et al. (2017). We note that there is nothing in our model which guarantees this interpretability, since depending on the retrieval could explain an observation as a combination of two spectra which incidentally provide the correct signature but are not actually present at the bottom. The R_b could thus be correct, even if the mixing fractions were not. Future work will evaluate the interpretability of these fractions; prior work in terrestrial ecology (Roberts et al., 2015) suggests that the spectroscopic measurement provides sufficient constraint to prevent nonphysical combinations. Investigators could easily create scene-specific libraries around their unique investigation objectives. Simply changing spectrum matching error metrics might also improve R_b class fidelity (Petit et al., 2017).

Acknowledgments

Carnegie Airborne Observatory imaging spectrometer data collection and pre-processing were funded by the Carnegie Institution for Science Ventures Program. The Carnegie Airborne Observatory is made possible by the Avatar Alliance Foundation, John D. and Catherine T. MacArthur Foundation, Grantham Foundation for the Protection of the Environment, Mary Anne Nyburg Baker and G. Leonard Baker Jr., and William R. Hearst III. We thank the members of the JPL PRISM team including Sarah Lundeen, Winston Olson-Duvall, and Joseph Renzullo. A portion of the research described in this paper was performed by the Jet Propulsion laboratory, California Institute of Technology, under a contract with the National Aeronautics and Space Administration. We acknowledge the support of the NASA Earth Science Division.

References

Ahmad, Z.Z., Franz, B.B., McClain, C.C., Kwiatkowska, E.E., Werdell, J.J., Shettle, E.E., Holben, B.B., 2010. New aerosol models for the retrieval of aerosol optical thickness and normalized water-leaving radiances from the seawifs and MODIS sensors over coastal regions and open oceans. Appl. Opt. 49, 5545–5560.

Andréfouët, S.S., Hochberg, E.J.E.J., Chevillon, C.C., Muller-Karger, F.E.F.E., Brock, J.C.J.C., Hu, C.C., 2007. Multi-scale remote sensing of coral reefs. Remote Sens. Coast. Aquat. Environ. 297–315.

Asner, G.P.G.P., Knapp, D.E.D.E., Boardman, J.J., Green, R.O.R.O., Kennedy-Bowdoin, T.T., Eastwood, M.M., Martin, R.E.R.E., Anderson, C.C., Field, C.B.C.B., 2012. Carnegie Airborne Observatory-2: increasing science data dimensionality via high-fidelity multi-sensor fusion. Remote Sens. Environ. 124, 454–465.

Asner, G.P.G.P., Knapp, D.E.D.E., Kennedy-Bowdoin, T.T., Jones, M.O.M.O., Martin, R.E.R.E., Boardman, J.J., Field, C.B.C.B., 2007. Carnegie Airborne Observatory: in-flight fusion of hyperspectral imaging and waveform light detection and ranging for three-dimensional studies of ecosystems. J. Appl. Remote. Sens. 1.

Bell, T.W.T.W., Cavanaugh, K.C.K.C., Siegel, D.A.D.A., 2015. Remote monitoring of giant kelp biomass and physiological condition: an evaluation of the potential for the hyperspectral infrared imager (HyspIRI) mission. Remote Sens. Environ. 167, 218–228 Special Issue on the Hyperspectral Infrared Imager (HyspIRI).

Biospherical Instruments Inc., 2011. Prr-800 Profiling Reflectance Radiometer. Product Technical Brochure. . www.biospherical.com.

Bishop, C.M.C.M., 2006. Pattern Recognition and Machine Learning. Springer.

Botha, E.J.E.J., Brando, V.E.V.E., Anstee, J.M.J.M., Dekker, A.G.A.G., Sagar, S.S., 2013. Increasedspectral resolution enhances coral detection under varying water conditions. Remote Sens. Environ. 131, 247–261.

Brando, V.E.V.E., Anstee, J.M.J.M., Wettle, M.M., Dekker, A.G.A.G., Phinn, S.R.S.R., Roelfsema, C.C., 2009. A physics based retrieval and quality assessment of bathymetry from suboptimal hyperspectral data. Remote Sens. Environ. 113, 755–770.

Breiman, L.L., 2001. Random forests. Mach. Learn. 45, 5–32.

Brown, L.D.L.D., Levine, M.M., et al., 2007. Variance estimation in nonparametric regression via the difference sequence method. Ann. Stat. 35, 2219–2232.

Bruckner, A.W.A.W., 2002. Life-saving products from coral reefs. Issues Sci. Technol. 18, 39–44.

Mark Eakin, C.C., Nim, C.J.C.J., Brainard, R.E.R.E., Aubrecht, C.C., Elvidge, C.C., Gledhill, D.K.D.K., Muller-Karger, F.F., Mumby, P.J.P.J., Skirving, W.J.W.J., Strong, A.E.A.E., Wang, M.M., Weeks, S.S., Wentz, F.F., Ziskin, D.D., 2010. Monitoring coral reefs from space. Oceanography.

Chauvaud, S.S., Bouchon, C.C., Maniere, R.R., 1998. Remote sensing techniques adapted to high resolution mapping of tropical coastal marine ecosystems (coral reefs, seagrass beds and mangrove). Int. J. Remote Sens. 19, 3625–3639.

Dekker, A.G.A.G., Phinn, S.R.S.R., Anstee, J.J., Bissett, P.P., Brando, V.E.V.E., Casey, B.B., Fearns, P.P., Hedley, J.J., Klonowski, W.W., Lee, Z.P.Z.P., et al., 2011. Intercomparison of shallow water bathymetry, hydro-optics, and benthos mapping techniques in Australian and Caribbean coastal environments. Limnol. Oceanogr. Methods 9, 396–425.

Dudhia, A.A., 2014. Oxford University Reference Forward Model (RFM). http://www.atm.ox.ac.uk/RFM/.
Frouin, R.R., Pelletier, B.B., 2015. Bayesian methodology for inverting satellite ocean-color data. Remote Sens. Environ. 159, 332–360.
Gao, B.C.B.C., Goetz, A.F.A.F., 1990. Column atmospheric water vapor and vegetation liquid water retrievals from airborne imaging spectrometer data. J. Geophys. Res. Atmos. 95, 3549–3564.
Gao, B.C.B.C., Heidebrecht, K.B.K.B., Goetz, A.F.A.F., 1993. Derivation of scaled surface reflectances from AVIRIS data. Remote Sens. Environ. 44, 165–178.
Garbow, B.B., Hillstrom, K.K., Moré, J.J., Moshier, S.S., Markwardt, C.C., 1980. MPFIT: A MINPACK-1 Least Squares Fitting Library in C. https://www.physics.wisc.edu/craigm/idl/cmpfit.html URL Accessed: July 2016.
Garcia, R.A.R.A., Hedley, J.D.J.D., Tin, H.C.H.C., Fearns, P.R.P.R., 2015. A method to analyze the potential of optical remote sensing for benthic habitat mapping. Remote Sens. 7, 13157–13189.
Goodman, J.A.J.A., Lee, Z.P.Z.P., Ustin, S.L.S.L., 2008. Influence of atmospheric and sea-surface corrections on retrieval of bottom depth and reflectance using a semi-analytical model: a case study in Kaneohe Bay, Hawaii. Appl. Opt. 47, F1–F11.
Green, R.O.R.O., Carrere, V.V., Conel, J.E.J.E., 1989. Measurement of atmospheric water vapor using the airborne visible/infrared imaging spectrometer. In: Proceedings of the ASPRS Conference on Image Processing, Reno, NV.
Gruninger, J.H.J.H., Ratkowski, A.J.A.J., Hoke, M.L.M.L., 2004. The sequential maximum angle convex cone (SMACC) endmember model. International Society for Optics and Photonics. pp. 1–14.
Guanter, L.L., Gómez-Chova, L.L., Moreno, J.J., 2008. Coupled retrieval of aerosol optical thickness, columnar water vapor and surface reflectance maps from envisat/meris data over land. Remote Sens. Environ. 112, 2898–2913.
Hamylton, S.S., 2011. Estimating the coverage of coral reef benthic communities from airborne hyperspectral remote sensing data: multiple discriminant function analysis and linear spectral unmixing. Int. J. Remote Sens. 32, 9673–9690.
Hedley, J.D.J.D., Mumby, P.P., Joyce, K.K., Phinn, S.S., 2004. Spectral unmixing of coral reef benthos under ideal conditions. Coral Reefs 23, 60–73.
Hedley, J.D.J.D., Roelfsema, C.M.C.M., Phinn, S.R.S.R., Mumby, P.J.P.J., 2012. Environmental and sensor limitations in optical remote sensing of coral reefs: implications for monitoring and sensor design. Remote Sens. 4, 271–302.
Hochberg, E.E., Bruce, C.C., Minnett, P.P., Green, R.R., Oaida, B.V.B.V., Muller-Karger, F.E.F.E., Gentemann, C.C., Mobley, C.D.C.D., Zimmerman, R.C.R.C., Park, Y.Y., Turner, W.W., Goodman, J.J., Gao, B.-C.B.-C., Knox, R.G.R.G., Middleton, E.M.E.M., Turpie, K.R.K.R., Ungar, S.S., 2011. HyspIRI sun glint report. Jet Propulsion Laboratory Publication, Jet Propulsion Laboratory, California Institute of Technology 11-4.
Hochberg, E.J.E.J., 2011. Remote Sensing of Coral Reef Processes. pp. 25–35.
Hochberg, E.J.E.J., Atkinson, M.J.M.J., Andréfouët, S.S., 2003. Spectral reflectance of coral reef bottom-types worldwide and implications for coral reef remote sensing. Remote Sens. Environ. 85, 159–173.
Hoegh-Guldberg, O.O., Mumby, P.J.P.J., Hooten, A.J.A.J., Steneck, R.S.R.S., Greenfield, P.P., Gomez, E.E., Harvell, C.D.C.D., Sale, P.F.P.F., Edwards, A.J.A.J., Caldeira, K.K., Knowlton, N.N., Eakin, C.M.C.M., Iglesias-Prieto, R.R., Muthiga, N.N., Bradbury, R.H.R.H., Dubi, A.A., Hatziolos, M.E.M.E., 2007. Coral reefs under rapid climate change and ocean acidification. 318. pp. 1737–1742.
Jay, S.S., Guillaume, M.M., 2014. A novel maximum likelihood based method for mapping depth and water quality from hyperspectral remote-sensing data. Remote Sens. Environ. 147, 121–132.
Keshava, N.N., Mustard, J.F.J.F., 2002. Spectral unmixing. IEEE Signal Process. Mag. 19, 44–57.
Klonowski, W.M.W.M., Fearns, P.R.P.R., Lynch, M.J.M.J., 2007. Retrieving key benthic cover types and bathymetry from hyperspectral imagery. J. Appl. Remote. Sens. 1 011505–011505-21.
Lee, Z.Z., Carder, K.L.K.L., Mobley, C.D.C.D., Steward, R.G.R.G., Patch, J.S.J.S., 1998. Hyperspectral remote sensing for shallow waters. I. a semianalytical model. Appl. Opt. 37, 6329–6338.
Lee, Z.Z., Carder, K.L.K.L., Mobley, C.D.C.D., Steward, R.G.R.G., Patch, J.S.J.S., 1999. Hyperspectral remote sensing for shallow waters: 2. deriving bottom depths and water properties by optimization. Appl. Opt. 38, 3831–3843.
Lewis, P.P., GÃşmez-Dans, J.J., Kaminski, T.T., Settle, J.J., Quaife, T.T., Gobron, N.N., Styles, J.J., Berger, M.M., 2012. An earth observation land data assimilation system (EO-LDAS). Remote Sens. Environ. 120, 219–235 The Sentinel Missions - New Opportunities for Science.
Maritorena, S.S., Morel, A.A., Gentili, B.B., 1994. Diffuse reflectance of oceanic shallow waters: influence of water depth and bottom albedo. Limnol. Oceanogr. 39, 1689–1703.
Mobley, C.C., Sundman, L.L., 2001. Hydrolight 4.2, Users Guide. Sequoia Scientific, Redmon, WA.
More, J.J.J.J., 1978. The Levenberg-Marquardt algorithm: implementation and theory. Numer. Anal. 105–116.
Mouroulis, P.P., Green, R.O.R.O., Van Gorp, B.B., Moore, L.B.L.B., Wilson, D.W.D.W., Bender, H.A.H.A., 2016. Landsat swath imaging spectrometer design. Opt. Eng. 55 (1) 015104–015104.
Mouroulis, P.P., Green, R.O.R.O., Wilson, D.W.D.W., 2008. Optical design of a coastal ocean imaging spectrometer. Opt. Express 16, 9087–9096.
Mouroulis, P.P., Van Gorp, B.B., Green, R.O.R.O., Dierssen, H.H., Wilson, D.W.D.W., Eastwood, M.M., Boardman, J.J., Gao, B.-C.B.-C., Cohen, D.D., Franklin, B.B., et al., 2014. Portable remote imaging spectrometer coastal ocean sensor: design, characteristics, and first flight results. Appl. Opt. 53, 1363–1380.
Mumby, P.J.P.J., Skirving, W.W., Strong, A.E.A.E., Hardy, J.T.J.T., LeDrew, E.F.E.F., Hochberg, E.J.E.J., Stumpf, R.P.R.P., David, L.T.L.T., 2004. Remote sensing of coral reefs and their physical environment. Mar. Pollut. Bull. 48, 219–228.
Nicholls, R.J.R.J., Wong, P.P.P.P., Burkett, V.V., Codignotto, J.J., Hay, J.J., McLean, R.R., Ragoonaden, S.S., Woodroffe, C.D.C.D., Abuodha, P.P., Arblaster, J.J., et al., 2007. Coastal systems and low-lying areas.
Petit, T.T., Bajjouk, T.T., Mouquet, P.P., Rochette, S.S., Vozel, B.B., Delacourt, C.C., 2017. Hyperspectral remote sensing of coral reefs by semi-analytical model inversion comparison of different inversion setups. Remote Sens. Environ. 190, 348–365.
Roberts, C.M.C.M., McClean, C.J.C.J., Veron, J.E.N.J.E.N., Hawkins, J.P.J.P., Allen, G.R.G.R., McAllister, D.E.D.E., Mittermeier, C.G.C.G., Schueler, F.W.F.W., Spalding, M.M., Wells, F.F., Vynne, C.C., Werner, T.B.T.B., 2002. Marine biodiversity hotspots and conservation priorities for tropical reefs. Science 295, 1280–1284.
Roberts, D.A.D.A., Dennison, P.E.P.E., Roth, K.L.K.L., Dudley, K.K., Hulley, G.G., 2015. Relationships between dominant plant species, fractional cover and land surface temperature in a Mediterranean ecosystem. Remote Sens. Environ. 167, 152–167.
Rodgers, C.D.C.D., 2000. Inverse methods for atmospheric sounding: theory and practice. 2.
Rothman, L.S.L.S., Gordon, I.E.I.E., Babikov, Y.Y., Barbe, A.A., Chris Benner, D.D., Bernath, P.F.P.F., Birk, M.M., Bizzocchi, L.L., Boudon, V.V., Brown, L.R.L.R., et al., 2013. The HITRAN2012 molecular spectroscopic database. J. Quant. Spectrosc. Radiat. Transf. 130, 4–50.
Shettle, E.P.E.P., 1990. Models of aerosols, clouds and precipitation for atmospheric propagation studies. Atmospheric propagation in the UV, visible, IR and mm-region and related system aspects. 14. pp. 15–32.
Stehman, S.V.S.V., 1997. Selecting and interpreting measures of thematic classification accuracy. Remote Sens. Environ. 62, 77–89.
Tanré, D.D., Deroo, C.C., Duhaut, P.P., Herman, M.M., Morcrette, J.J.J.J., Perbos, J.J., Deschamps, P.Y.P.Y., 1990. Technical note description of a computer code to simulate the satellite signal in the solar spectrum: the 5s code. Int. J. Remote Sens. 11, 659–668.
Teillet, P.M.P.M., 1989. Surface reflectance retrieval using atmospheric correction algorithms. In: Geoscience and Remote Sensing Symposium, IGARSS'89. 12th Canadian Symposium on Remote Sensing. 2. pp. 864–867.
Thompson, D.R.D.R., Gao, B.-C.B.-C., Green, R.O.R.O., Roberts, D.A.D.A., Dennison, P.E.P.E., Lundeen, S.R.S.R., 2015a. Atmospheric correction for global mapping spectroscopy: {ATREM} advances for the HyspIRI preparatory campaign. Remote Sens. Environ. 167, 64–77.
Thompson, D.R.D.R., Seidel, F.C.F.C., Gao, B.C.B.C., Gierach, M.M.M.M., Green, R.O.R.O., Kudela, R.M.R.M., Mouroulis, P.P., 2015b. Optimizing irradiance estimates for coastal and inland water imaging spectroscopy. Geophys. Res. Lett. 42, 4116–4123.
Turpie, K.R.K.R., Klemas, V.V.V.V., Byrd, K.K., Kelly, M.M., Jo, Y.-H.Y.-H., 2015. Prospective HyspIRI global observations of tidal wetlands. Remote Sens. Environ. 167, 206–217 Special Issue on the Hyperspectral Infrared Imager (HyspIRI).
Vermote, E.F.E.F., Tanré, D.D., Deuze, J.L.J.L., Herman, M.M., Morcette, J.J.J.J., 1997. Second simulation of the satellite signal in the solar spectrum, 6s: an overview. IEEE Trans. Geosci. Remote Sens. 35, 675–686.
Wasserman, L.L., 2007. All of Nonparametric Statistics. Springer, New York.
White, A.T.A.T., Vogt, H.P.H.P., Arin, T.T., 2000. Philippine coral reefs under threat: the economic losses caused by reef destruction. Mar. Pollut. Bull. 40, 598–605.
Wozencraft, J.J., Lillycrop, W.W., 2002. Total shallow water survey through shoals lidar. In: Proceedings of Oceanology International.
Yuhas, R.H.R.H., Goetz, A.F.H.A.F.H., Boardman, J.W.J.W., 1992. Discrimination among semi-arid landscape endmembres using the spectral angle mapper (SAM) algorithm. In: Summaries 3rd Annual JPL Airborne Geoscience Workshop. 1. pp. 147149.
Zoffoli, M.L.M.L., Frouin, R.R., Kampel, M.M., 2014. Water column correction for coral reef studies by remote sensing. Sensors 14 (9), 16881–16931.